

Intense Vorticity Structures in Newtonian Turbulence and Turbulent Dissipation in Viscoelastic Fluids Analyzed by Direct Numerical Simulations

Afonso Silva Resende de Avelar Ghira
afonso.ghira@tecnico.ulisboa.pt

Instituto Superior Técnico, Universidade de Lisboa, Portugal

July 2019

Abstract

This work intends to study the features of intense vorticity structures (IVS) in Newtonian turbulence and also aims to provide a survey related to turbulent dissipation in viscoelastic turbulence. Both approaches are based in direct numerical simulations (DNS) of forced homogeneous and isotropic turbulence (HIT) at statistically steady state conditions. The former case explores numerically those structures for a wider range of Reynolds numbers than those found in the literature, namely $88 < Re_\lambda < 429$. In general, statistics confirm previous results from other authors, like the scalabilities of the radius of those structures, R_{ivs} , with Kolmogorov's length scale η and of their azimuthal velocity, at a distance R_{ivs} , with the velocity root-mean-square u' . However, the length of IVS was found to be scalable with η , bringing a new result in this field of research. The latter survey depicts the differences inherent to the elastic degrees of freedom, characterizing viscoelastic fluids, by comparing the spectral dynamics of the kinetic energy evolution equation of a purely viscous fluid, modeled with Carreau-Yasuda, and a viscoelastic one, simulated with FENE-P, when imposing the same shear-thinning behavior. Furthermore, still regarding the FENE-P constitutive rheological model, tests were conducted to support the scalability law between the β concentration and Weissenberg number, at the onset of dissipation reduction, predicted by de Gennes's theory. Finally, a preliminary study about a possible presence of a Virk's-like asymptote was developed near maximum dissipation reduction conditions.

Keywords: Direct Numerical Simulations, Intense Vorticity Structures, FENE-P, Homogeneous and Isotropic Turbulence, Viscoelasticity

1. Introduction

Mastering turbulent phenomenon is crucial for engineering conceptualization and, in particular, for aerospace applications. Thus, a phenomenological research in turbulence through Direct Numerical Simulations (DNS) is conducted in this work.

Dynamics of vortical structures is inherently linked with kinetic energy production and dissipation, mixing, diffusion, and transport of mass, heat and momentum. The study of these structures is also encouraged by their simplicity, being the knowledge of their mechanisms a prerequisite for flow prediction and control, [1, 2].

Since the work published by Toms [3] on drag reduction in solutions with polymer additives, the phenomenon has been surveyed and gained many practical applications and research work. Nowadays, it has application, *e.g.*, in long-distance liquid transporting in pipeline facilities. In research field, heat transfer features of viscoelastic fluids have re-

cently been studied, *e.g.*, in cooling applications for turbine disks [4], and it may constitute a possible application for aerospace industry.

To simulate viscoelastic fluids, the Finitely Extensible Nonlinear Elastic model with Peterlin closure (FENE-P) is used. An analogy may be made among this set of equations and that for Magneto-Hydrodynamics (MHD), [5]. Plasma flows are now part of a set of new technologies that takes place in hypersonic propulsion so, for aerospace industry, plasma flows simulated with MHD have inherent relevance, [6].

This work aims to investigate IVS as well as turbulent dissipation with polymer additives in forced Homogeneous and Isotropic Turbulence, (HIT), at statistically steady state conditions. They are analyzed with DNS. First, IVS will be analyzed for several Reynolds numbers to give statistical results for higher Reynolds numbers and a scalability law for their length. Then, turbulence will be simulated

with the Carreau-Yasuda (CY) model to assess the capability, of a purely viscous flow, of reproducing the dynamics of viscoelastic turbulence, simulated with FENE-P, when applied the same shear-thinning law. Just regarding the FENE-P model, the onset of dissipation reduction DR will be investigated to find the scalability law between polymer β concentration and Weissenberg number We at those conditions. Finally, still with the viscoelastic model, this time simulated near maximum DR conditions, it will be provided a preliminary survey for the behavior of dissipation coefficient C_ϵ and a preliminary assessment of a possible presence of a Virk's-like asymptote.

2. Background

2.1. Homogeneous and Isotropic Turbulence

The view of turbulent scale-to-scale interactions can be developed by considering the two-point correlation function, R_{ij} , which is defined as,

$$R_{ij}(\vec{x}, \vec{r}, t) \equiv \langle u_i(\vec{x} + \vec{r}, t) u_j(\vec{x}, t) \rangle, \quad (1)$$

where $\vec{x} \equiv (x_1, x_2, x_3)$ is the positioning vector and $\vec{r} \equiv (r_1, r_2, r_3)$ represents a vector displacement relative to \vec{x} . Here $\langle \cdot \rangle$ represents ensemble averaging. The dependence on time will be omitted for simplicity. Restrictions may be made on R_{ij} . If turbulence is homogeneous equation (1) reduces to be just dependent on \vec{r} so $R_{ij}(\vec{x}, \vec{r}, t) = R_{ij}(\vec{r}, t)$. Apart from homogeneity, there are further restrictions that might be made. In particular, an isotropic symmetry condition may be imposed. If the tensor is homogeneous and isotropic, it has the form,

$$R_{ij}(\vec{r}) = u'^2 \left(g(r) \delta_{ij} + (f(r) - g(r)) \frac{r_i r_j}{r^2} \right), \quad (2)$$

where $f(r)$ and $g(r)$ are scalar-valued functions dependent on $r = \sqrt{r_i r_i}$. Here, δ_{ij} is the Kronecker Delta and $R_{ij}(0) = \langle u_i u_j \rangle = u'^2 \delta_{ij}$. Those functions can be related for an incompressible turbulent field by the continuity equation, which states that $\partial R_{ij} / \partial x_j = 0$, leaving just one unknown to be determined. By their construction, f is called the longitudinal autocorrelation function and g the transverse one.

A Fourier Transform can be performed and the resulting isotropic tensor \widehat{R}_{ij} is fully characterized by a scalar-valued function dependent on the wavenumber norm k . That scalar function can be the so-called energy spectra \widehat{E} , which provides the information of the contribution of each wavenumber to the root mean square of the velocity fluctuation. Mathematically one has,

$$R_{ij}(\vec{r}) = \sum_{\vec{k}} \widehat{R}_{ij}(\vec{k}) e^{i2\pi \vec{k} \cdot \vec{r} / \mathcal{L}}, \quad (3)$$

where $\vec{k} \equiv (k_1, k_2, k_3) \in \mathbb{Z}^3$ is the wavenumber vector and R_{ij} is assumed periodic with period \mathcal{L} .

The Fourier Transform \widehat{R}_{ij} can be shown to be $\widehat{R}_{ij}(\vec{k}) = \langle \hat{u}_i(\vec{k}) \hat{u}_j(-\vec{k}) \rangle$. The energy spectrum $\widehat{E}(k)$, function with a discrete domain, is defined as,

$$\widehat{E}(k) = \sum_{\vec{k}'} \frac{1}{2} \widehat{R}_{ii}(\vec{k}') \delta_{k',k}, \quad (4)$$

where $k = \sqrt{k_i k_i}$. Note that the kinetic energy $K = \langle u_i u_i \rangle / 2 = R_{ii}(0) / 2 = \sum_k \widehat{E}(k)$.

In HIT, Kolmogorov's scales are well defined due to the tight dependence of the statistics on ν and ϵ in the dissipation range, where ν is the kinematic viscosity and ϵ the dissipation rate. Those scales are $\eta \equiv (\nu^3 / \epsilon)^{1/4}$, $u_\eta \equiv (\nu \epsilon)^{1/4}$ and $\tau_\eta \equiv (\nu / \epsilon)^{1/2}$, the Kolmogorov's length, velocity and time scales, respectively.

Further references are important to give to characteristic scales widely used to describe turbulent motion. For a characteristic length, which large scales scale with, it is defined,

$$L_{11} = \frac{1}{2} \int_0^{\mathcal{L}} f(r) dr = \frac{\pi}{2u'^2} \sum_k \frac{\widehat{E}(k)}{2\pi k / \mathcal{L}}, \quad (5)$$

and it is called the longitudinal length scale. It describes motions with velocities scalable with u' . The Taylor microscale is defined as $\lambda = (-f''(0))^{-1/2}$. In HIT it reduces to $\lambda^2 = 15\nu u'^2 / \epsilon$. In turbulence, the Taylor microscale-based Reynolds number is commonly used and is defined as $Re_\lambda = u' \lambda / \nu$.

In HIT, $\lambda^2 / \eta^2 = \sqrt{15} Re_\lambda = 15 u'^2 / u_\eta^2$ and $L_{11} / \eta = 15^{-3/4} Re_\lambda^{3/2}$ considering $\epsilon \sim u'^3 / L_{11}$.

These features may be seen in [7].

2.2. Coherent Vorticity Structures in Turbulent Field

In turbulence, coherent vorticity structures have been studied for some years. They consist in regions with concentrated vorticity and with a lifetime compared with that of large scales.

In HIT, intense vorticity structures (IVS) are particular coherent structures which have strong vorticity. Topologically they are characterized by swirling slender tubular vortices, reason for being known as 'worms'. These structures are identified by means of a vorticity magnitude threshold ω_{ivs} . Jiménez defined that as being the vorticity magnitude above which the flow points with the highest enstrophy represent 1% of the total, [8]. A study about the features of these structures in isotropic turbulence have been given relevance by many researchers, *e.g.* [9, 8, 10].

The IVS have been studied in other types of flows such as mixing layers [11], channel flows [12] and jets [2]. So far, similar statistics were presented for these type of structures independently of the nature of the flow considered and the tracking methods used.

Some usual statistics are defined to characterize the worms. A Gaussian distribution profile is assumed and used to fit the vorticity, $\omega_z(\mathbf{r}) = \omega_0 e^{-r^2/R_{ivs}^2}$, where ω_0 is the vorticity at the axis and R_{ivs} is the worm radius estimated with the fit. Then, through the relation given by the Stokes' Theorem for a circulation at a distance R_{ivs} , a mean equivalent azimuthal velocity is obtained as $U_{ivs} = 0.316\omega_0 R_{ivs}$. The characteristic circulation of the worm is then $\Gamma = U_{ivs}2\pi R_{ivs}$, and the worm circulation-based Reynolds number is defined as $Re_\Gamma = \Gamma/\nu$. The length of worm L_{ivs} is defined by the end-to-end distance that the direct detection method computes. With these quantities defined, the mean values are taken and the statistics are then $\langle R_{ivs} \rangle$, $\langle U_{ivs} \rangle$ and $\langle L_{ivs} \rangle$.

The results obtained by some authors are given in table 1 and are used for comparison.

In order to give simple explanations and predictions about the dynamics of IVS, the Burgers' Vortex Model is often used. It describes a steady and axisymmetric vortex tube subject to a strain field oriented towards its vorticity vector. The relevance of using this model is related to the fact that for an applied strain rate the smallest flow features one should expect to generate are of the order of the Burgers' radius R_B [8]. To assess if this model can describe IVS, their local radius are compared to the local R_B . So far, it has been concluded for IVS that $R_{ivs} \sim R_B$ and that their azimuthally averaged vorticity profiles are approximately Gaussian, (consistent with Burgers' model), showing that those structures can be modeled as equilibrium Burgers' vortices [8, 10].

The length of IVS has not been neither studied over a large range of Re_λ nor systematically measured over the available range. The majority of the references to it are mostly based in visual inspection of those structures embedded in the flow. Some quantitative measurements were given by Jiménez in [8], based on a direct detection method, and he said that L_{ivs} scales with L_{11} , [8]. In a later work, Jiménez has also given measurements by a direct detection method, see table 1, saying that L_{ivs} scales with L_{11} and that $\mathcal{O}(L_{ivs}) = \mathcal{O}(L_{11})$, [10]. Based on an integration of normalized auto-correlation functions of properties of the filaments, Jiménez in [10] gave also other measurements.

2.3. Complex Fluids and Turbulence with Polymer Additives

So far, the classical Newtonian constitutive model for the stresses was considered.

A complex fluid which can still be modeled as having a viscous response to forces is purely viscous. One of the most popular models for shear-thinning fluids is the Carreau-Yasuda viscosity model, [13].

On the other hand, viscoelastic fluids have both

viscous and elastic responses to forces. The FENE-P (Finitely Extensible Nonlinear Elastic with Peterlin closure) model will be used to simulate polymer additives in this work.

Regarding turbulence with polymer additives, the many experiments available at that time allowed Virk to start to compile and analyze it more systematically. His work in [14], showed a region where no drag reduction is identified and a Maximum Drag Reduction (MDR) region characterized by a universal asymptote, independent of the system and polymer properties, limiting the amount of drag reduction, see figure 1.

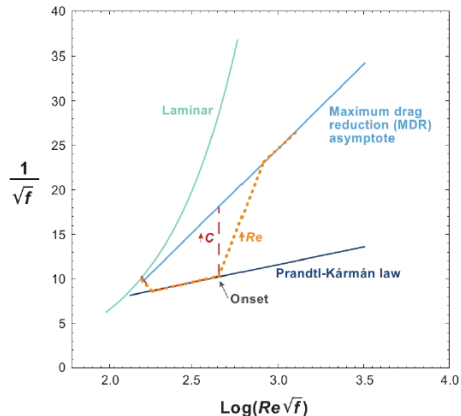


Figure 1: Modified skin friction $f^{-1/2}$ as a function of modified Reynolds number $\log(Re f^{1/2})$, (Prandtl-Kármán coordinates). From [15].

A theory based on elastic arguments was proposed by de Gennes [16]. He postulated that the elastic energy stored by partially stretched polymers, (function of polymer concentration), interferes with the Newtonian energy cascade influencing drag reduction.

Sreenivasan in [17] used this theory to test its prediction for the onset of drag reduction when adapted to pipe flows. Sreenivasan argued that the usage of de Gennes' theory might be justified at least for two reasons. First, measurements have shown that drag reduction depends systematically on polymer concentration and, secondly, experiments have suggested that partial stretching is perhaps the rule. The fact that de Gennes' theory is based on HIT along with those reasons make it suitable for this work.

Consider HIT at a high Reynolds number, away from walls, and a length scale ℓ^* in the inertial subrange. Now let the corresponding characteristic time scale be equal to the polymer relaxation time τ_p , $\tau^* = \tau_p = (\ell^{*2}/\epsilon)^{1/3}$. The elastic theory postulates that polymers can be stretched by scales $\ell < \ell^*$. Furthermore, it states that there is a range

Flow	Ref.	Re_λ	$\langle R_{ivs} \rangle / \eta$	$\langle R_{ivs} / R_B \rangle$	$\langle U_{ivs} \rangle / u'$	$\langle U_{ivs} \rangle / u_\eta$	$Re_\Gamma / Re_\lambda^{1/2}$	$\langle L_{ivs} \rangle / L_{11}$	$\langle L_{ivs} \rangle / \eta$
F. I.	[8]	36–168	3.8–4.2	—	—	—	16.5–21.1	2.60–3.16	94.80–570.24
	[10]	37–168	4.8–4.9	0.92–1.05	0.86–0.99	—	—	2.2–2.8	58.6–310.9
	[1]	46	3.2–3.8	—	—	—	14.7–32.4	—	—
	[2]	111	4.6	0.99	0.68	9.0	28.8	—	—
D. I.	[10]	62	4.8	0.82	1.21	—	—	3.2	184.0
S.	[1]	—	4.9–5.2	—	—	—	—	—	—
M. L.	[11]	80–100	4.5	—	0.50	—	—	—	—
C. F.	[12]	200–380	4.0–5.0	—	—	1.2–2.0	—	—	—

Table 1: Statistics of IVS. The flow types are Forced Isotropic Turbulence (F. I.), Decaying Isotropic Turbulence (D. I.), Homogeneous Shear (S.), Mixing Layer (M. L.) and Channel Flow (C. F.). The various Re_λ in [12] were estimated with the available data. Table and caption adapted from [2].

of scales $\ell' < \ell < \ell^*$ where polymers are stretched little. Even more, although scales $\ell < \ell^*$ affect polymers, scales $\ell' < \ell$ remain unaffected by polymers. The scale ℓ' is such that the elastic energy K_{el} stored by the polymers (per unit volume) matches the turbulent kinetic energy (per unit volume) at that scale. The $K_{el}(\ell)$ depends on the stretching at that scale $\zeta(\ell) = (\ell^*/\ell)^q$, where q depends on the dimensionality of the stretching, being 1 in two dimensions and 2 in three dimensions. For the elastic energy one has, $K_{el} = nk_B T \zeta^{5/2}$, where n is the number density of polymer molecules, k_B is the Boltzmann constant and T is the absolute temperature. So far one has,

$$\rho(\epsilon\ell')^{2/3} \sim nk_B T \left(\frac{\tau_p}{\tau'} \right)^{15q/4}. \quad (6)$$

On the onset conditions one should expect that $\ell' = \eta$ and $\tau' = \tau_\eta$. Introducing the Weissenberg number $We \equiv \tau_p / \tau_\eta$, the polymer concentration parameter β and the relation $nk_B T = (1 - \beta) \mu^{[s]} / (\tau_p \beta)$, where $\mu^{[s]}$ is the solvent dynamic viscosity, on the onset one has,

$$\frac{(1 - \beta)}{\beta} \sim We^{1-15q/4}. \quad (7)$$

Note that the solvent kinematic viscosity $\nu^{[s]} = \mu^{[s]} / \rho$.

3. Governing Equations and Numerical Methods

Navier-Stokes equations in Cartesian coordinates, for a velocity field with an average of zero, for incompressible fluid at constant properties in its generalized form can be read as,

$$\frac{\partial u_i}{\partial x_i} = 0, \quad (8a)$$

$$\frac{\partial u_i}{\partial t} + \frac{\partial}{\partial x_j} (u_i u_j) = -\frac{1}{\rho} \frac{\partial p}{\partial x_i} + \frac{1}{\rho} \frac{\partial T_{ij}}{\partial x_j}. \quad (8b)$$

Here u_i is the fluctuating velocity field, p is the pressure and the stress tensor T_{ij} is prescribed according with the three constitutive equations needed in the present work.

3.1. Constitutive Models

The three closures treated are descriptors of the so-called Newtonian, Carreau-Yasuda or polymeric fluids.

For a Newtonian fluid one has, $T_{ij} = 2\mu S_{ij}$, where S_{ij} is the rate-of-strain tensor given by, $S_{ij} = (\partial u_i / \partial x_j + \partial u_j / \partial x_i) / 2$.

For the Carreau-Yasuda one has $T_{ij} = 2\mu_c (S_{rm} S_{rm}) S_{ij}$ where,

$$\begin{aligned} \mu_c &= \mu_\infty \\ &+ (\mu_0 - \mu_\infty) \left(1 + \left(\lambda_c \sqrt{2S_{ij} S_{ij}} \right)^a \right)^{\frac{n_c - 1}{a}}. \end{aligned} \quad (9)$$

Here μ_c is again the kinematic viscosity, μ_0 is that when $S_{ij} S_{ij} = 0$ while μ_∞ when $S_{ij} S_{ij} \rightarrow \infty$. On the other hand, λ_c , a and n_c are parameters defining the curve.

For the FENE-P first consider the way the conformation tensor C_{ij} is defined. This tensor is symmetric positive definite (SPD). Considering R_i the vector representing the relative displacement of two beads in one dumbbell, one has, $C_{ij} \equiv \langle R_i R_j \rangle / (\langle R_k R_k \rangle_{eq} / 3)$. Its transport equation is,

$$\begin{aligned} \frac{\partial C_{ij}}{\partial t} + u_k \frac{\partial C_{ij}}{\partial x_k} &= \frac{\partial u_j}{\partial x_k} C_{ik} + \frac{\partial u_i}{\partial x_k} C_{jk} \\ &- \frac{1}{\tau_p} (f(C_{kk}) C_{ij} - \delta_{ij}), \end{aligned} \quad (10)$$

where $f(C_{kk}) \equiv (L^2 - 3) / (L^2 - C_{kk})$ is the Peterlin function and L is the non-dimensional maximum extensibility. To couple equation (10) with the system (8) it is mandatory to give a closure for T_{ij} . So, $T_{ij} = T_{ij}^{[s]} + T_{ij}^{[p]}$, with the superscript $[s]$ standing for solvent and $[p]$ for polymer

stresses. Solvent stresses are modeled as Newtonian, $T_{ij}^{[s]} = 2\mu^{[s]}S_{ij}$, and polymer stresses are given by $T_{ij}^{[p]} = (1 - \beta)\mu^{[s]}(f(C_{kk})C_{ij} - \delta_{ij})/(\beta\tau_p)$.

3.2. Numerical Methods

To solve numerically Navier-Stokes equations, a pseudo-spectral method is used spatially (with periodic boundary conditions), in a cubic box with a side of 2π meters. For temporal integration, a 3rd-order accurate Runge-Kutta scheme is used. Initial conditions are set so one has a Gaussian energy spectrum at $t = 0$ and, in the case of FENE-P, $C_{ij}(\vec{x}, 0) = \delta_{ij}$. For Newtonian and Carreau-Yasuda simulations $CFL < 3/5$. On the other hand, for FENE-P simulations, not only for stability purposes, but also to guarantee symmetry and positive definitiveness, $CFL < 1/6$, see [18] for proof of SPD conservativeness. The solution for \hat{u}_i , the Fourier Transform of u_i , is de-aliased according to the 2/3 rule. In this work, the simulations performed are forced in order to develop a turbulent field. The forcing method follows that described by [19]. It is a volume random forcing made divergence free, so it does not influence the pressure directly, delta-autocorrelated in time, once it is considered as white noise, and uncorrelated with the velocity, the latter due its random nature, see [19].

Navier-Stokes equations in Fourier space are read as,

$$\frac{\partial \hat{u}_i}{\partial t} - P_{ik} \frac{ik_j \hat{T}_{kj}}{\rho} = -P_{ik} \hat{G}_k, \quad (11)$$

where the projection tensor $P_{ik} = (\delta_{ik} - k_i k_k / k^2)$ and $\hat{G}_k = ik_j \widehat{u_k u_j}$. Here $\widehat{(\cdot)}$ represents the Fourier Transform of the respective variable.

The transport equation for C_{ij} is spatially discretized in a different way. The convection term $u_k \partial C_{ij} / \partial x_k$ is discretized with the Kurganov-Tadmor (KT) method to ensure SPD properties everywhere. Its nodal value is approximated by its mean value all over a finite cell surrounding a generic grid point i, j and k , following a finite volume method. Second-order accurate spatial derivatives are used whenever SPD is guaranteed. If not, the method changes to first-order accurate. The stretching term $\partial u_j / \partial x_k C_{ik} + \partial u_i / \partial x_k C_{jk}$ is discretized spatially using a second-order central differences method to approximate velocity gradients. The details are described in [18].

In the next section the results and discussion will be presented.

4. Results and Discussion

4.1. Intense Vorticity Structures Characterization

To understand how the characteristics evolve with Reynolds, several simulations were made, where $88 < Re_\lambda < 429$. The resolution used was $k_{max}\eta = 2$. The conditional statistics made on IVS

were made using the Wormtracker code. The results obtained are shown in table 2.

Case	N	Re_λ	ϵ [m^2/s^3]	ν [m^2/s]	L_{11} [m]	u' [m/s]	$\langle L_{ivs} \rangle / \eta$
A	256	90	10.00	0.0145	0.89	2.98	49.24
B	512	145	10.00	0.0057	0.84	2.99	52.18
C	768	198	10.55	0.0034	0.89	3.11	54.44
D	1024	248	9.66	0.0022	0.91	3.07	57.96
E	1536	312	10.57	0.0014	0.85	3.10	58.06
F	2048	429	9.90	0.0009	0.88	3.23	57.18
G	2048	292	9.90	0.0009	0.60	2.67	57.81

Table 2: Simulations Parameters. N is the number of mesh points in each direction.

One of the primary results ever looked at is the scalability of R_{ivs} with η . In this case it was obtained $R_{ivs} \approx 4\eta$ with convergence for higher Reynolds, in agreement with other results, see table 1. Other result of major importance when modeling such structures is the capability of doing so by the Burgers' Vortex model. The average value of local R_{ivs} with respect to local R_B is $\langle R_{ivs} / R_B \rangle \approx 0.98$, in agreement with other authors, see table 1. The accuracy of this model to predict the radius allows one to infer that IVS might be seen as locally steady Burgers' Vortexes. Even for values away from the mean, PDF's, (not shown), show that extreme values are still close to unity.

The characteristic azimuthal velocity U_{ivs} is of the order and scalable with the large scale characteristic velocity u' . If $\langle U_{ivs} \rangle \sim u'$, one should expect that $\langle U_{ivs} \rangle / u_\eta \sim Re_\lambda^{1/2}$. That was explored and confirmed, showing that $\langle U_{ivs} \rangle / u' \approx 0.85$, in agreement with previous results, see table 1.

One of the answers this work intends to provide is the scalability law for $\langle L_{ivs} \rangle$. First consider figure 2. For several Reynolds, two plots of the PDF's are shown, one of them in figure 2(a) for $\langle L_{ivs} \rangle / L_{11}$ and other, in figure 2(b), for $\langle L_{ivs} \rangle / \eta$. Inspection

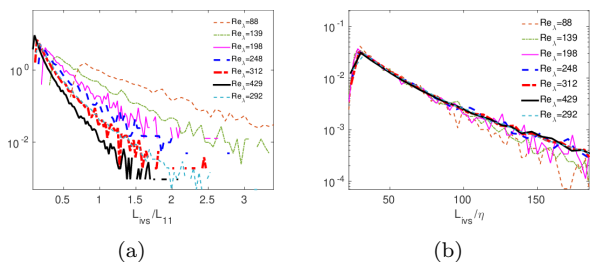


Figure 2: Scalability tests for $\langle L_{ivs} \rangle$ (a) with L_{11} and (b) with η .

of the former, due to the lack of collapsing, shows no great support to the scalability with L_{11} . However, exploring the latter, a possible scalability with this smaller characteristic length is present. To clarify this, one can simultaneously test the scalability

with respect to one variable and the lack of it with respect to another. For $Re_\lambda > 120$, if $\langle L_{ivs} \rangle \sim \eta$, one should expect that $\langle L_{ivs} \rangle / L_{11} \sim Re_\lambda^{-3/2}$. Figure 3 shows this behavior, confirming that $\langle L_{ivs} \rangle$ scales with η . It also gives a picture of the scalability trend directly with η . Note that convergence

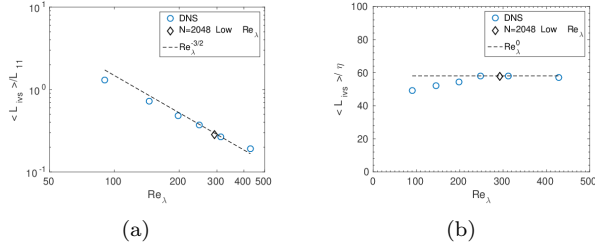


Figure 3: Scalability laws for (a) $\langle L_{ivs} \rangle / L_{11}$ and (b) $\langle L_{ivs} \rangle / \eta$.

is only attained at $Re_\lambda > 250$. The other statistics shown so far, usually converge for $Re_\lambda > 120$. It was found that $\langle L_{ivs} \rangle \approx 58\eta$. The simulation in black in these figures indicate the result for simulation G. The importance of this simulation arises to confirm that there are no confinement influences. In order to reach higher Reynolds, the forcing was concentrated at lower wavenumbers, which in turn increases L_{11} . When L_{11} is too high, due to the periodicity of the box, confinement can influence the solution. Simulation G, with low L_{11} and thus, low Re_λ , represents a situation with no confinement. As G confirms the trend, it is safe to say that the other simulations, (with higher L_{11}), are confinement-free. Note as well that simulation G is right after the convergence threshold for this statistic. If there was confinement in the solutions, in order to achieve higher Reynolds, with a lower L_{11} , bigger mesh sizes would be needed.

4.2. Carreau-Yasuda and FENE-P Comparative Survey

In this section a comparative survey is performed. After prescribing the rheological parameters for FENE-P, those for the CY model may be determined. It is done by describing the viscosity induced by the polymer through the CY shear-dependent relation. The method uses the solution of FENE-P equations subjected to a imposed uniform shear flow with $\partial u_1 / \partial x_2 = \mathcal{S}$ and the remaining entries equal to 0, (Pinho, private communication).

Considering the CY model, for convenience, ν_c is decomposed according to $\nu_c = \nu_\infty + \tilde{\nu}$. Thus, $\partial \hat{E}(k) / \partial t$ can be shown to be,

$$-P_{ik} \mathfrak{R} \left\{ \underbrace{\hat{G}_k \hat{u}_i^*}_{T(k)} \right\} + \mathfrak{R} \left\{ \underbrace{\hat{M}'_i u_i^*}_{L(k)} \right\} - \underbrace{2\nu_\infty k^2 \hat{E}(k)}_{D(k)} + H(k), \quad (12)$$

where \hat{M}'_i is the fluctuating term corresponding

to the contribution of $\tilde{\nu}$ and $H(k)$ is the forcing spectrum. Summing the terms in this latter equation over all k gives $\partial K / \partial t = -\tilde{\epsilon} - \epsilon_\infty + P$, where $\sum_k \hat{E}(k) = K$, $\sum_k T(k) = 0$, $\sum_k L(k) = -\tilde{\epsilon}$, $\sum_k D(k) = \epsilon_\infty$ and $\sum_k H(k) = P$. The cumulative transfer term is also defined as $\Pi(k) \equiv -\sum_{k'}^k T(k')$.

For the FENE-P case $\partial \hat{E}(k) / \partial t$ is equal to,

$$-P_{ik} \mathfrak{R} \left\{ \underbrace{\hat{G}_k \hat{u}_i^*}_{T(k)} \right\} + \mathfrak{R} \left\{ \underbrace{\hat{M}'_i u_i^*}_{T_p(k)} \right\} - \underbrace{2\nu^{[s]} k^2 \hat{E}(k)}_{D(k)} + H(k), \quad (13)$$

where \hat{M}'_i is the term arising from the elastic component. The term $T_p(k)$ represents the power transferred from the polymer to the solution. Summing the terms in this latter equation over all k gives $\partial K / \partial t = -\epsilon^{[p]} - \epsilon^{[s]} + P$, where $\sum_k T_p(k) = -\epsilon^{[p]}$ and $\sum_k D(k) = -\epsilon^{[s]}$.

The parameters chosen for FENE-P and the results of the curve fitting for CY are seen in table 3. For all simulations the viscosities were set to $\nu = \nu^{[s]} = \nu_\infty = 0.0023$. The viscosity ν refers to that used in the Newtonian reference simulation. The Newtonian reference simulation has its char-

FENE-P				
Case	L	τ_p [s]	β	$\nu^{[s]}$ [m^2/s]
F1	100	0.025	0.8	0.0023
F2	100	0.050	0.8	0.0023
F3	100	0.100	0.8	0.0023
F4	100	0.200	0.8	0.0023
Carreau-Yasuda				
Case	a	n_c	λ_c [s]	ν_0 [m^2/s]
C1	1.9422	0.5163	0.0007	0.0029
C2	1.8758	0.4767	0.0013	0.0029
C3	1.7903	0.4416	0.0023	0.0029
C4	1.7084	0.4156	0.0043	0.0029

Table 3: Constitutive Parameters for comparison between FENE-P and Carreau-Yasuda models.

acteristics summarized in table 4. In all simulations the mesh size in each direction N was kept constant, as well as the power input P . Reference

N	Re_λ	P [m^2/s^3]	u' [m/s]
768	181	10	2.7

Table 4: Simulation Parameters for the Newtonian case.

conditions are computed with results from the Newtonian simulation. Table 5 summarizes the results from the FENE-P simulations. The results from Carreau-Yasuda simulations can be checked in table 6. Figures show quantities non-dimensionalized by Newtonian statistics.

First consider the energy spectra at statistically steady state conditions, which can be seen on fig-

Case	We^{ref}	We	τ_p [s]	$\epsilon^{[s]}$ [m^2/s^3]	$\epsilon^{[p]}$ [m^2/s^3]	DR [%]	u' [m/s]
F1	2	1	0.025	7.05	2.95	30	2.7
F2	3	2	0.050	3.87	6.13	61	2.6
F3	7	3	0.100	2.00	8.00	80	2.5
F4	13	5	0.200	1.19	8.81	88	2.3

Table 5: Simulations Parameters for the FENE-P cases.

Case	λ_c [s]	ϵ_∞ [m^2/s^3]	$\tilde{\epsilon}$ [m^2/s^3]	u' [m/s]
C1	0.0007	8.03	1.97	2.6
C2	0.0013	7.79	2.21	2.7
C3	0.0023	7.83	2.17	2.6
C4	0.0043	8.04	1.96	2.7

Table 6: Simulations Parameters for the Carreau-Yasuda cases.

ure 4. Figure 4(b) shows the energy spectra for

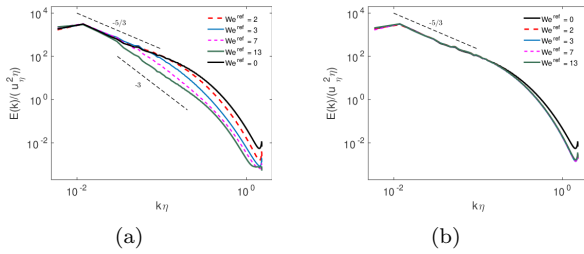


Figure 4: $E(k)/(u_\eta^2 \eta)$ (a) for all FENE-P cases and (b) for all Carreau-Yasuda cases. Both have the Newtonian spectra.

the CY cases. Kolmogorov's Second Similarity Hypothesis is expected to hold, once, with sufficiently high Reynolds number, a universal region with local $Re_\ell \gg Re_\eta$ might be encountered such that it is independent from ν_c . Figure 4(a) shows what happens when FENE-P is considered instead. It is clearly evident the influences in the cascade are increasingly felt up through the Newtonian inertial range as We^{ref} increases. For high We^{ref} , power flux is redirected through the polymer. When it happens, the slope of -3 in the energy cascade appears.

The forcing spectra $H(k)$ is concentrated at low wavenumbers, being zero for $k\eta > k_h\eta = 2 \times 10^{-2}$. Spectra with respect to each type of fluid will be denoted with a subscript C , N or F , whenever it refers to Carreau-Yasuda, Newtonian or FENE-P type of fluid. Numbers that might appear in the subscript as well refer to each case for each type of fluid.

In figure 5, which shows the cumulative transfer spectra $\Pi(k)$, it should be noted that $\max \Pi_N = P$ after $H(k)$ becoming zero. As long as $\Pi_N \approx P$, $D_N \approx 0$. Figure 5(a) shows that a Newtonian-like inertial range is present in

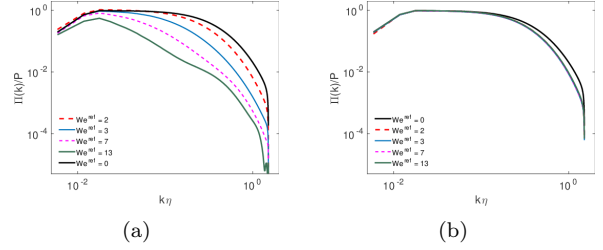


Figure 5: $\Pi(k)/P$ (a) for all FENE-P cases and (b) for all Carreau-Yasuda cases. Both have the Newtonian spectra.

Carreau-Yasuda cases. Furthermore, it is clear that $\int (D_N(k) - D_C(k)) = \tilde{\epsilon}$. Consider k_1 as the wavenumber where a FENE-P curve in figure 5(a) departs from the Newtonian one or, if it does not reach the Newtonian curve, take $k_1 = k_h$. Now, considering the summation,

$$\begin{aligned}
0 &= \sum_k^{k_1} T_F(k) + \sum_k^{k_1} T_P(k) - \sum_k^{k_1} D_F(k) + \sum_k^{k_1} H(k) \\
&= -\underbrace{\Pi_F(k_1)}_{\leq P} - \Pi_P(k_1) - \underbrace{\sum_k^{k_1} D_F(k)}_{\leq \sum_k^{k_1} D_N(k) \approx 0} + P \quad (14) \\
&\geq -P - \Pi_P(k_1) + P,
\end{aligned}$$

one has $\Pi_P(k_1) \geq 0$. This latter relation indicates that k_1 is the wavenumber where the flux of energy is being redirected through polymer motion.

Figure 6 shows the case $F4$ in comparison with the case $C4$, along with the Newtonian curve. In

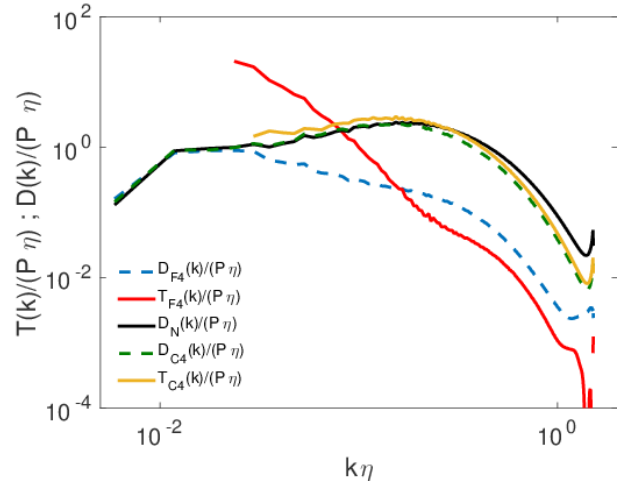


Figure 6: $D(k)/(P\eta)$ and $T(k)/(P\eta)$ for both cases $F4$ and $C4$. The $D(k)/(P\eta)$ is also provided for the Newtonian case, which equals $T(k)/(P\eta)$ at steady state for $k\eta > 2 \times 10^{-2}$.

the case $F4$ the high value of $T_{F4}(k)$ clearly indicates that the energy flux given to the largest scales is being almost all redirected to polymer motion.

Indeed, for $k\eta \geq k_h\eta$, $T_{F4}(k) - D_{F4}(k) = -T_p(k)$ and, for $T_{F4} - D_{F4} > 0$, $T_p < 0$, which means that the energy flux flows from solvent to polymer. On the other hand, when $T_{F4} - D_{F4} < 0$, $T_p > 0$, which means that some flux of energy is flowing from polymer back to the solvent.

4.3. Dissipation Reduction Onset and Preliminary Study Near Maximum Dissipation Reduction

This section will provide an additional survey in what concerns polymer induced phenomenon.

As a reference for this study, as usual, Newtonian simulations are also performed. The Newtonian reference simulation is that with resolution equal to the reference resolution, $(k_{max}\eta) = (k_{max}\eta)^{ref}$, and equal mesh size. In a FENE-P simulation, $(k_{max}\eta)^{ref}$ is computed with the total dissipation rate and solvent kinematic viscosity so $(k_{max}\eta)^{ref} = N(\nu^{[s]3}/P)^{1/4}/3$. Likewise, τ_η^{ref} is determined accordingly to define We^{ref} . On the other hand, Re_λ^{ref} is that resultant from the Newtonian simulation. For all FENE-P simulations, $(k_{max}\eta)^{ref} = 1.5$. So, for given power input P and mesh size in each direction N , the viscosity is set.

For the onset of dissipation reduction two Re_λ^{ref} will be used. Then, a set of $(\beta; \tau_p)$ pair values is chosen.

Near maximum dissipation reduction, one Re_λ^{ref} will be used. Then, as well, a set of $(\beta; \tau_p)$ pair values is chosen different from the previous one. Analogously to the skin friction, the dissipation coefficient is considered. It is defined as, $C_\epsilon = \epsilon^{[s]}L_{11}/u^{*3}$. The Reynolds number used will be Re_λ , computed from solvent quantities as well.

In all simulations, the non-dimensional maximum extensibility L is kept constant.

Consider figure 7. For two Re_λ^{ref} , dissipation reduction is plotted as a function of $(1 - \beta)/\beta$ and We^{ref} . Those plots are bi-logarithmic and show re-

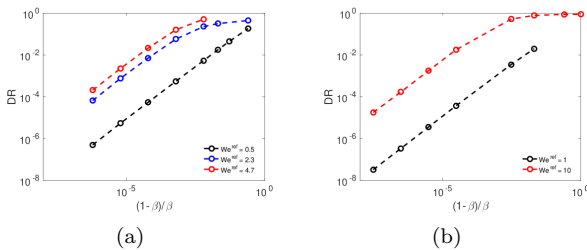


Figure 7: Dissipation reduction DR as a function of $(1 - \beta)/\beta$ at various We^{ref} (a) for $Re_\lambda^{ref} = 67$ and (b) for $Re_\lambda^{ref} = 91$. These samples are at the onset of dissipation reduction.

gions with a constant slope for each We^{ref} . If one is trying to find a power law between $(1 - \beta)/\beta$ and We^{ref} while expecting a power law when relating DR with $(1 - \beta)/\beta$, a region on those plots

showing parallel straight lines indicates the onset region. So, taking a set of points at constant DR in the onset region one can test the scalability law $(1 - \beta)/\beta \sim We^\delta$. Figure 8 shows the results for both Re_λ^{ref} . The plot shows $(1 - \beta)/\beta$ as a function of We for a constant $DR = 1 \times 10^{-3}$. The

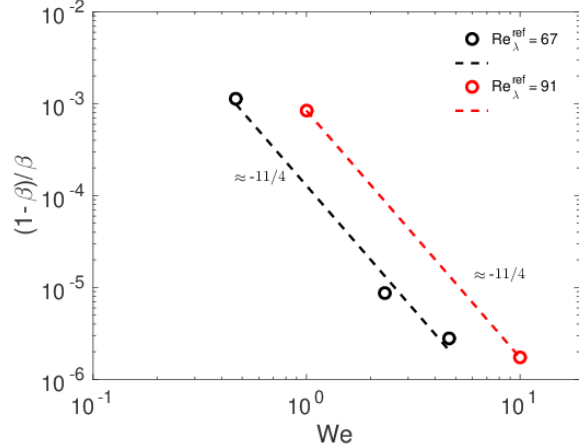


Figure 8: Scalability law for the onset of DR . The fitted slope indicates a value of $\approx -11/4$, resulting in a stretching exponent $q \approx 1$.

curves shown represent linear regressions for the set of points used. Both slopes are approximately equal and are taken equal to $\delta \approx -11/4$. In equation (7), where $\delta = 1 - 15q/4$, a q in the exponent was left to be determined. With the present result, $q \approx 1$, representing a bi-dimensional stretching. In pipe flow, Sreenivasan [17] determined a corresponding value of $\approx 2/3$. In forced homogeneous and isotropic turbulence that value was expected to be higher, due to no geometrical confinement by the boundaries.

In pipe flow it is commonly seen that, for a given Reynolds, no matter the polymer properties, there is a maximum drag reduction limit. To study this behavior in HIT, an analogy needs to be made first. A logical one is to consider the dissipation reduction phenomenon. The dissipation coefficient C_ϵ and Re_λ are considered. The parameters used to non-dimensionalize both C_ϵ and Re_λ are important to note, however, that vary under an addition of polymers. So, due to this fact, it is important to clarify that dissipation reduction and dissipation coefficient reduction are not necessarily equivalent. Figure 9 shows the results obtained for DR and C_ϵ both as a function of $(1 - \beta)/\beta$ and We^{ref} . It is not considered $\beta < 0.5$ due to the fact that it represents the region where polymers overlap, being $\beta = 0.5$ of the order of the limit when polymers begin to overlap. Both figures also show that maximum dissipation reduction and minimum C_ϵ for each We^{ref} are approximately equal among them for each dissipation statistic, suggesting saturation both for increasing

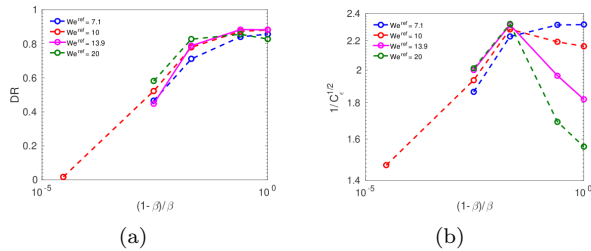


Figure 9: Dissipation statistics as a function of $(1 - \beta)/\beta$ for various We^{ref} , (a) represents DR and (b) represents $1/C_\epsilon^{1/2}$. A sample near Newtonian conditions, ($DR \approx 0$), is also given.

$(1 - \beta)/\beta$ and We^{ref} . The smooth convergence to a possible global maximum DR and to a possible global minimum C_ϵ may indicate that a region independent from polymer properties may be present. Figure 10 shows the results of C_ϵ as a function of Re_λ . That relation is shown in Prandtl-Kármán

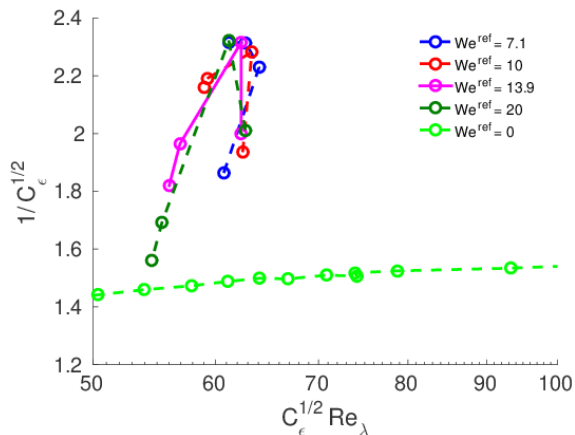


Figure 10: Relation between C_ϵ and Re_λ for various We^{ref} and β in Prandtl-Kármán coordinates. The lines joining the samples follow an ascending order of $(1 - \beta)/\beta$, being the lowest, (the starting point), in the lower-right corner, (considering the set of points with $We^{ref} \neq 0$).

coordinates, $C_\epsilon^{-1/2} - C_\epsilon^{1/2} Re_\lambda$. It also represents the Newtonian curve, the $We^{ref} = 0$ curve. The maximum deviation from the Newtonian curve in both plots seems to converge independently from the polymer properties.

5. Conclusions

5.1. Achievements

DNS of several cases regarding different subjects were conducted. First, Newtonian simulations were performed to study the characteristics of IVS for higher Reynolds numbers. Then a comparative study between a purely viscous fluid, simulated with the Carreau-Yasuda model, and a viscoelastic fluid, simulated with the FENE-P model, for the same

shear-thinning behavior, took place. Finally, a survey with respect to FENE-P alone was done concerning turbulent dissipation features.

Newtonian simulations performed regarding the study of IVS brought numerical results for forced HIT for Re_λ up to 429, greater than those found in literature, see table 1. It allowed to confirm scalability laws already presented such as $\langle R_{ivs} \rangle \approx 4\eta$, $\langle R_{ivs} \rangle \approx 0.98R_B$, $\langle U_{ivs} \rangle \approx 0.85u'$. The major achievement refers to the scalability law for $\langle L_{ivs} \rangle$, which was shown to be $\langle L_{ivs} \rangle \sim \eta$. It was verified that although $\langle L_{ivs} \rangle$ can attain values $\mathcal{O}(L_{11})$, it scales, in fact, with η .

The comparative survey was important to depict the rather different dynamics underlying each phenomenon. Basically, in the CY case, by an assessment of the kinetic energy evolution equation at statistically steady state conditions, Newtonian-like spectra for scales greater than the smallest were seen. Indeed, an agreement with Kolomogorov's Second Similarity Hypothesis was expected to see, as the local Reynolds number Re_ℓ increases upwards the cascade, and a viscosity-independent dynamics that becomes relevant. On the other hand, FENE-P dynamics showed that the elastic mechanism alters deeply the spectra. Spectra assessments revealed that the FENE-P elastic mechanism, even for high Re_λ , might be felt from the inertial range up to the energy-containing range, becoming, this influence, specially stronger as We^{ref} increases. Comparing statistics like $\tilde{\epsilon}$ with $\epsilon^{[p]}$ or ϵ_∞ with $\epsilon^{[s]}$ clearly denotes that the strain correlation structure is largely different between these fluid cases.

Finally, numerical experiments with the FENE-P model were done to explore the onset of dissipation reduction and the C_ϵ behavior near maximum dissipation reduction conditions. For the former, de Gennes' theory was tested, specifically the scalability law $(1 - \beta)/\beta \sim We^{1-15p/4}$, which it predicts at onset conditions. The results for two Re_λ^{ref} indicate a probable We exponent $1 - 15p/4 \approx -11/4$, giving the stretching exponent p a value $p \approx 1$. This p value, as expected, was found to be greater than that for pipe flow. According to Sreenivasan [17], that value, (for pipe flow), was determined to be $p \approx 2/3$. So, the scaling found, (for HIT), is of the form $(1 - \beta)/\beta \sim We^{-11/4}$. For the latter case, which constitute itself a preliminary study of Virk's-like asymptote in forced HIT, showed, for one Re_λ^{ref} , approximately the same limiting C_ϵ value by β and We^{ref} variations. As a smooth convergence to a possible limiting value for C_ϵ is present, for the Re_λ^{ref} tested, it may indicate that a region independent from polymer properties may be present.

5.2. Future Work

For future work some ideas are purposed as follows.

Still regarding the IVS, a deeper study about their stability with increasing Re_λ may be done to understand how IVS remain stable, due to the fact that Re_Γ also increases.

Further explore the possible presence of a Virk's-like asymptote in forced HIT.

Explore the behavior of passive scalars, *e.g.*, heat, in viscoelastic fluids.

Begin to look at turbulence with MHD dynamics, as it is largely different from classical turbulence, specially in what it concerns to small scale statistical structure.

Acknowledgements

I would like to emphasize my thankfulness for the unswerving support and confidence in me of Professor Carlos Silva during these years.

Some words of gratitude should be given to Professor Fernando Pinho for the useful advices he gave me.

I want also to state my acknowledgment to my friend Hugo Abreu for the worthwhile discussions about several subjects.

No words of acknowledgment should be left unsaid to my friend Nuno Pimentel, who showed astonishing skills in Project Management when he helped me to schedule the writing process of my thesis.

Special thanks are naturally entangled with my deep love for my Mother Myriam, Dad João and my Sister Inês.

References

- [1] S. Kida and H. Miura. Identification and analysis of vortical structures. *Eur. J. Mech. (B/Fluids)*, 17(4):471–488, 1998.
- [2] C. B. da Silva, R. J. N. Reis, and J. C. F. Pereira. The intense vorticity structures near the turbulent/non-turbulent interface in a jet. *J. Fluid Mech.*, 685:165–190, 2011.
- [3] B. A. Toms. Some observations on the flow of linear polymers solutions through straight tubes at large reynolds numbers. In *Proc. 1st Intern. Congr. Rheol.*, pages 135–141, North Holland, Amsterdam, 1948.
- [4] A.S. Dogonchi and D.D. Ganji. Investigation of heat transfer for cooling turbine disks with a non-newtonian fluid flow using dra. *Case Studies in Thermal Engineering*, 6:40–51, 2015.
- [5] A. Fouxon and V. Lebedev. Spectra of turbulence in dilute polymer solutions. *Physics of Fluids*, 15(7):2060–2072, 2003.
- [6] R. Jousot, S. Coumar, and V. Lago. Plasmas for high speed flow control. *Plasmas for Aeronautics*, 10(AL10-04), 2015.
- [7] S. B. Pope. *Turbulent Flows*. Cambridge University Press, 2000.
- [8] Javier Jiménez, Alan A. Wray, Philip G. Saffman, and Robert S. Rogallo. The structure of intense vorticity in isotropic turbulence. *J. Fluid Mech.*, 225:65–90, 1993.
- [9] Eric D. Siggia. Numerical study of small-scale intermittency in three-dimensional turbulence. *J. Fluid Mech.*, 107:375–406, 1981.
- [10] Javier Jiménez and Alan A. Wray. On the characteristics of vortex filaments in isotropic turbulence. *J. Fluid Mech.*, 373:255–285, 1998.
- [11] M. Tanahashi, S. Iwase, and T. Miyauchi. Appearance and alignment with strain rate of coherent fine scale eddies in turbulent mixing layer. *J. Turbul.*, 2(6):1—17, 2001.
- [12] S.-J. Kang, M. Tanahashi, and T. Miyauchi. Dynamics of fine scale eddy clusters. *J. Turbul.*, 8(52):1–19, 2007.
- [13] S. E. Spagnolie, editor. *Complex Fluids in Biological Systems: Experiment, Theory and Computation*. Springer, 2015.
- [14] P. S. Virk, E. W. Merrill, H. S. Mickley, K. A. Smith, and E. L. Mollo-Christensen. The toms phenomenon: turbulent pipe flow of dilute polymer solutions. *J. Fluid Mech.*, 20:22–30, 1967.
- [15] C. M. White and M. G. Mungal. Mechanics and prediction of turbulent drag reduction with polymer additives. *Annu. Rev. Fluid Mech.*, 40:235–256, 2008.
- [16] P. G. De Gennes. *Introduction to Polymer Dynamics*. Cambridge University Press, 1990.
- [17] K. R. Sreenivasan and C. M. White. The onset of drag reduction by dilute polymers and maximum drag reduction asymptote. *J. Fluid Mech.*, 409:149–164, 2000.
- [18] T. Vaithianathan, A. Robert, J. G. Brasseur, and L. R. Collins. An improved algorithm for simulating three-dimensional, viscoelastic turbulence. *J. Non-Newt. Fluid Mech.*, 140(1):3–22, 2006.
- [19] K. Alvelius. Random forcing of three-dimensional homogeneous turbulence. *Phys. Fluids*, 11(7):1880–1889, 1999.